Carbon 208 (2023) 421–431

Contents lists available at ScienceDirect

Carbon

journal homepage: www.elsevier.com/locate/carbon

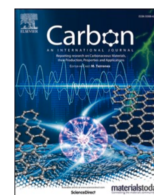

Boron-doped diamond by 9 MeV microbeam implantation: Damage and recovery

R.J. Jiménez-Riobóo [a], N. Gordillo [b,c,d], A. de Andrés [a,*], A. Redondo-Cubero [b,c,d], M. Moratalla [b,d,e], M.A. Ramos [b,d,e,**], M.D. Ynsa [b,c]

[a] Instituto de Ciencia de Materiales de Madrid (ICMM-CSIC), 28049, Madrid, Spain
[b] Centro de Microanálisis de Materiales (CMAM), Universidad Autónoma de Madrid, 28049, Madrid, Spain
[c] Departamento de Física Aplicada, Universidad Autónoma de Madrid, 28049, Madrid, Spain
[d] Instituto Nicolás Cabrera, Universidad Autónoma de Madrid, 28049, Madrid, Spain
[e] Departamento de Física de la Materia Condensada, Condensed Matter Physics Center (IFIMAC), Universidad Autónoma de Madrid, 28049, Madrid, Spain

ARTICLE INFO

Keywords:
Diamond crystal
Raman spectroscopy
Ion-beam irradiation
Boron-doped diamond
Damage recovery
Ion beam modification of materials

ABSTRACT

Diamond properties can be tuned by doping and ion-beam irradiation is one of the most powerful techniques to do it in a controlled way, but it also produces damage and other aftereffects. Of particular interest is boron doping which, in moderate concentrations, causes diamond to become a p-type semiconductor and, at higher boron concentrations, a superconductor. Nevertheless, the preparation of superconducting boron-doped diamond by ion implantation is hampered by amorphization and subsequent graphitization after annealing. The aim of this work was to explore the possibility of creating boron-doped diamond superconducting regions and to provide a new perspective on the damage induced in diamond by MeV ion irradiation. Thus, a comprehensive analysis of the damage and eventual recovery of diamond when irradiated with 9 MeV B ions with different fluences has been carried out, combining Raman, photoluminescence, electrical resistivity, X-ray diffraction and Rutherford Backscattering/Ion-channeling. It is found that, as the B fluence increases, carbon migrates to interstitial sites outside of the implantation path and an amorphous fraction increases within the path. For low fluences ($\sim 10^{15}$ ions/cm^2), annealing at 1000 °C is capable to fully recovering the diamond structure without graphitization. However, for higher fluences ($\geq 5 \times 10^{16}$ ions/cm^2), those required for superconductivity, the recovery is important, but some disorder still remains. For high fluences, annealing at 1200 °C is detrimental for the diamond lattice and graphite traces appear. The incomplete healing of the diamond lattice and the interstitial location of B can explain that optimally doped samples do not exhibit superconductivity.

1. Introduction

Diamond is one of the materials of greatest technological and scientific interest due to its outstanding physical, chemical and structural properties [1,2]. As it is well known, diamond crystal is the hardest naturally occurring solid, it has an extremely high Young's modulus and Debye temperature, a low thermal expansion coefficient, and strikingly combines an excellent electrical insulation with the highest thermal conductivity [1]. The latter transport properties are very sensitive to impurity atoms. Strictly speaking, pure diamond is a very wide bandgap (5.5 eV) semiconductor, with a negligible concentration of intrinsic carriers at room temperature. Diamond can be doped with boron, which acts as an electron acceptor with an activation energy of 0.37 eV. When introducing boron concentrations of $n_B \sim 10^{17}$–10^{19} cm^{-3}, a significant number of holes are produced in the valence band and, consequently, diamond works as a *p*-type semiconductor [3–5]. So far, semiconductor applications in diamond have focused almost exclusively on boron-doped *p*-type diamond, for example, optoelectronic devices [6] and high-power and radiation-proof photoelectronic devices [7].

More recently, it was found that, above a metal-insulator transition [8,9] occurring for n_B on the order of 4.5×10^{20} cm^{-3}, boron-doped diamond (BDD) can exhibit superconductivity at low temperatures. This was firstly reported [10] in BDD crystallites grown by high-pressure, high-temperature (HPHT) techniques with $n_B \sim 4.6 \times$

* Corresponding author.
** Corresponding author. Centro de Microanálisis de Materiales (CMAM), Universidad Autónoma de Madrid, 28049, Madrid, Spain.
E-mail addresses: ada@icmm.csic.es (A. de Andrés), miguel.ramos@uam.es (M.A. Ramos).

https://doi.org/10.1016/j.carbon.2023.04.004
Received 3 February 2023; Received in revised form 1 April 2023; Accepted 3 April 2023
Available online 6 April 2023
0008-6223/© 2023 The Authors. Published by Elsevier Ltd. This is an open access article under the CC BY-NC-ND license (http://creativecommons.org/licenses/by-nc-nd/4.0/).

10^{21} cm^{-3} (i.e., ~2.6% of atomic boron concentration) and a critical temperature $T_c \leq 4K$. Soon afterwards, several works reported superconductivity in thin films usually grown by chemical vapor deposition (CVD) methods, with T_c ranging 1−10K and boron concentrations estimated to be (0.9−3.1) × 10^{21} cm^{-3} [11–14], including claims of superconducting behaviour below $T_c \approx 25K$ in higher-quality diamond crystals [14]. Nevertheless, other studies in polycrystalline BDD samples have shown the presence of granular superconductivity apparently uncorrelated with boron concentration [15,16]. Further, indications of superconductivity have also been reported in boron-doped carbon nanotubes [17], with $T_c = 12K$ for 1.5 at.% of boron, and in different phases of so-called amorphous Q-carbon, ranging from $T_c = 36K$ for 17 at.% boron to $T_c = 55K$ for 27 at.% boron [18,19]. The origin of superconductivity in BDD and its microscopic details are therefore far from well established.

Among the different preparation methods employed to obtain superconducting BDD, ion-beam implantation has not yet been sufficiently explored, in clear contrast to its use to make *semiconducting* BDD [3–5]. In fact, a few attempts have been reported [8,20,21], but have not been successful. Ion-beam implantation is generally an efficient method to selectively dope parts or regions of materials, although its use in diamond has its own particularities, which cannot be overlooked. In principle, the type of defects created by MeV implantation consists of well-defined localized defects and involves only a few atoms and consequently they can be annealed out very efficiently, leaving an almost pristine diamond [22]. Increasing the fluence, electronic damage effects produced by swift-heavy-ion irradiation in diamond crystals have been shown to be negligible for electronic stopping powers <14 keV/nm, but the damage originated from the nuclear stopping power is able to produce an appreciable amorphization [23,24]. Furthermore, diamond is a metastable allotrope of carbon at usual pressures and temperatures. Thus, when irradiating ions into diamond, if the density of generated defects exceeds a threshold value [25–27], after a high-temperature annealing the amorphized region transforms into graphite, the most stable allotrope of carbon, instead of healing the defects back to crystalline diamond as usually desired.

The graphitization threshold, however, depends on the ion implantation depth, which is related to the ion implantation energy and the ion type. Previous works with ion implantation energies of a few tens or hundreds of keV (corresponding to ion ranges below 1 μm), found a graphitization threshold of ~1 × 10^{22} vacancies/cm^3 [25–27]. Nevertheless, this value clearly increases for ion implantation depths of a few micrometres, corresponding to ion energies well above 1 MeV. The reason for this appears to be that when the damaged/amorphized diamond is deeply buried, the high internal pressures prevent their relaxation from sp^3 to sp^2 graphitically-bonded structures. Specifically, the required internal expansion for graphitization of the amorphized area is conditioned by the thickness of the surrounding diamond cap with much higher density [21,28–32]. For implantation depths of few micrometres, graphitization threshold values of 1.1 × 10^{23} vacancies/cm^3 [29] and 9 × 10^{22} vacancies/cm^3 [30] have been reported using 3 MeV and 2 MeV He^+ ions, respectively. Previous studies using boron or carbon ions suggested that even higher graphitization thresholds of vacancy density in diamond could be reached [33–35].

Despite the abovementioned drawbacks to perform strong boron doping in diamond (>1 at.%) using ion beams, that implies employing fluences above 1 × 10^{16} ions/cm^2, it can also offer big advantages. With MeV ion implantation, both the ionic implantation fluence and the modified region are accurately controlled. In particular, the boron implantation employing a focused ion beam allows doping only in the regions of interest, with micrometric or submicrometric dimensions, and the combination of different ion energies, can enable the manufacture of 3D devices with important technological applications. Especially, highly-focused boron MeV implantation could be an interesting technology for the manufacture of *p*-type semiconducting and superconducting microdevices. Some studies of the electrical behaviour after boron implantation, although using a non-focused beam, have already been carried out. The implantation of 2 MeV boron ions has allowed the formation of deeply buried electrically active boron doped layers in natural diamond, taking advantage of the high pressures existing inside the buried layer to allow annealing without graphitization [5,36,37].

Therefore, it is worth to study in more detail the effects produced by boron irradiation with higher energies and using a highly-focused ion beam, as well as to explore the possibility of creating superconducting regions in the diamond crystals after irradiating boron ions with high enough energies and fluences. In this work, single-crystalline diamond plates have been implanted with a focused 9 MeV ^{11}B ion beam under different fluences, as to produce and study different micrometric stripes of BDD.

In section 2, we briefly describe the various experimental methods that we have employed in this investigation. Two-dimensional Raman maps were carried out at and around the irradiated zones to determine the distribution of changes brought about by boron implantation, as well as after post-irradiation sequential annealing at 1000 °C and at 1200 °C. The electrical resistivity as a function of temperature was studied for the most relevant cases, for both annealing temperatures, to investigate its potential superconductivity. In addition, characterization techniques such as X-ray diffraction (XRD) and Rutherford Backscattering Spectrometry combined with ion channelling (RBS/C) were conducted to study the structural modification of the samples. Then, in section 3 we present and discuss the most relevant experimental results obtained with those techniques. In the last section, we summarize our findings and conclusions, providing an outlook of possible research lines to be followed in the near future.

2. Materials and methods

2.1. Samples and ion-beam irradiation

Diamond crystals were irradiated using the internal (high vacuum) microbeam line of a 5 MV electrostatic accelerator of tandem type in the Center for Micro Analysis of Materials (CMAM) at the Universidad Autónoma de Madrid (UAM) [38]. The focused ion beam employed had a size of about 5 × 3 μm^2 and a beam current of ~500 pA. The followed focalization procedure was similar to the one previously described [39].

The samples studied were mainly high-purity (Electronic Grade) type IIa single-crystalline diamond plates (2.0 mm × 2.0 mm × 0.5 mm), grown by CVD techniques by Element Six™ [40]. Concentrations of nitrogen and boron impurities are reported to be below 5 ppb and 1 ppb, respectively. According to specifications, the average surface roughness of the crystals is Ra <5 nm for the polished faces and Ra <200 nm for the unpolished faces.

A focused ion beam of $^{11}B^{3+}$ at 9 MeV was irradiated on above-mentioned single crystals. Hence, the penetration of the boron ion beam in the diamond sample was about 5 μm, as detailed in section 2.2. Different irradiations were conducted using fluences in the range 1.1 × 10^{15}−1.0 × 10^{17} ions/cm^2 (see Table 1). As a reference, stripe #6 corresponds to the boron concentration typically found in the best superconducting crystals reported [11–14]. The irradiated areas showed a grey color due to the created defects, the darkening being obviously stronger for the highest fluences (see Fig. 1). The ion beam direction was set perpendicular to an unpolished lateral (001) face of the diamond plate and then scanned fully crossing from one of the main (100) faces to the other forming parallel buried stripes 25 μm × 500 μm each. Therefore, a cross section of the irradiated layers at different depths could be optically accessed from one of the large polished faces of the sample. Other irradiations and measurements were also performed in several crystals of the same kind obtaining very similar results. Thus, in this work we will focus only on the most systematic and consistent study carried out with the sample shown in Fig. 1.

Table 1
Stripes labelling and fluence values of 9 MeV $^{11}B^{3+}$ ions implanted in the diamond sample and the corresponding concentration of implanted boron and density of vacancies, obtained from SRIM simulation. In both cases, the peak values at the stopping layer (at a depth of 4.96 μm) and more realistic average values in the region near the peak (±0.05 μm) are given.

Stripe #	Fluence (10^{14} cm^{-2})	Peak density of implanted B (10^{20} cm^{-3})	Average density of B near the ion range (10^{20} cm^{-3})	Peak density of vacancies (10^{22} cm^{-3})	Average density of vacancies near the ion range (10^{22} cm^{-3})
1	11	0.88	0.73	0.84	0.72
2	26	2.07	1.72	1.99	1.71
3	57	4.55	3.77	4.37	3.74
4	130	10.4	8.61	9.97	8.53
5	190	15.2	12.6	14.6	12.5
6	500	39.9	33.1	38.4	32.8
7	750	59.8	49.7	57.5	49.2
8	1000	79.8	66.2	76.7	65.6

2.2. Monte-Carlo simulations

In order to determine the theoretical concentration of implanted boron and the density of vacancies, Monte-Carlo simulations were carried out with the SRIM-2013 software [41]. The simulations were run in the "Detailed calculation with full damage cascades" mode by setting a displacement energy of 52 eV. These simulations show that 9 MeV boron ions penetrate the diamond to a depth of about 5.0 μm. Specifically, the concentration of implanted boron presents a maximum at 4.96 μm (see Fig. 2 and Table 1): the Bragg peak. The density of vacancies reflects the magnitude of lattice damage. Fig. 2 also shows the depth profiles of vacancy density for the different employed fluences. These profiles were calculated with a simple linear approximation without considering concurrent complex processes such as self-annealing, ballistic annealing and defect-defect interaction. However, the estimated damage density can be still regarded as a reliable first-order approximation to assess the lattice damage produced.

2.3. Thermal treatments

Annealing of the irradiated samples was carried out employing a quartz tube inside a horizontal furnace. Previously, the diamond crystal was placed in a homemade vacuum-sealed quartz ampoule, which was carefully purged and then typically kept with 100–200 mbar of Ar gas at room temperature. Slow heating and cooling ramps were then performed (more than 3.5 h each) with a dwell of 1 h for 1000 °C anneals and of 30 min for 1200 °C anneals.

2.4. Micro-Raman and micro-photoluminiscence

Micro-Raman experiments were performed using the 488 nm and 532 nm laser lines for the detection of the diamond Raman peak located at 1332 cm^{-1} and any features around this peak that could arise due to the irradiation of the sample, including photoluminescence (PL) bands. An Olympus microscope with a ×100 objective with a high optical aperture (N.A. = 0.95) allows for <0.8 μm lateral resolution. The scattered light was filtered with notch filters and analyzed with a Horiba (iHR-320) monochromator (1200 l/mm grating) coupled to a Peltier cooled Synapse CCD. A schema of the measurement configuration is presented in Fig. 1 (c−e). The regions irradiated with the eight different boron fluence values were mapped with 1 μm steps in the x and y directions and a total area of about 60 × 15 $μm^2$ (red rectangle, 915 spectra) for each region, the origin of the y axis being the surface of the diamond. The integrated areas of the relevant peaks are then obtained and shown as Raman intensity maps. The Raman maps of peak positions are obtained from the fits of the 915 spectra corresponding to each stripe. As said, the boron irradiation was performed on a lateral 500 μm-wide side of the diamond. So, to observe the impact in the depth of the diamond, the Raman spectra were obtained scanning the front surface in areas large enough (60 μm) to largely cover the 25 μm-wide irradiated areas and up to 15 μm from the edge, since the boron is calculated to be implanted at around 5 μm deep (see Fig. 2b). The Raman maps were performed at three stages: after irradiation, then after a first annealing (1000 °C) and finally after a second annealing (1200 °C). In order to differentiate between phonons and photoluminescence processes in the obtained spectra, two different excitation lasers have been used in some particular cases: 488 nm and 532 nm.

2.5. Electrical characterization at low temperatures

The electrical resistivity of some selected irradiated stripes after annealing was measured in a ^4He cryostat, using the typical four-probe method. 50 μm gold wires were welded on the stripe ends with silver paint. Low currents up to 1 μA were applied. The specific resistivity coefficients were determined from the measured resistance curves by considering for the stripes a homogenous cross section of 25 μm × 0.2

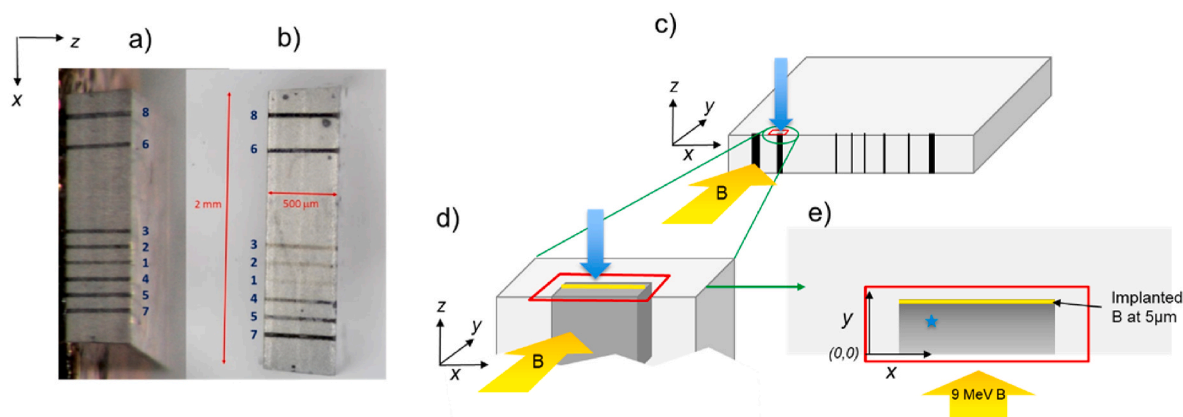

Fig. 1. Pictures of the main studied diamond crystal irradiated with 9 MeV B ions, showing the different stripes produced at different fluences, with the labels as indicated in Table 1. (a) Just after irradiation. (b) The same sample after the annealing at 1200 °C. (c) Scheme of the irradiated, lateral side of the diamond and (d and e) zooms showing the scanned area with micro-Raman (red rectangle) for one of the implanted stripes. The boron beam (yellow arrows) was parallel to y axis, scanning in the z direction across the thickness (0.5 mm) of the diamond sample. The laser direction and spot are shown in blue, the implanted boron (at around 5 μm from the surface) is represented as a yellow line and the path of B in grey. The axes and their origin (0,0) used in Raman maps are indicated. (A colour version of this figure can be viewed online.)

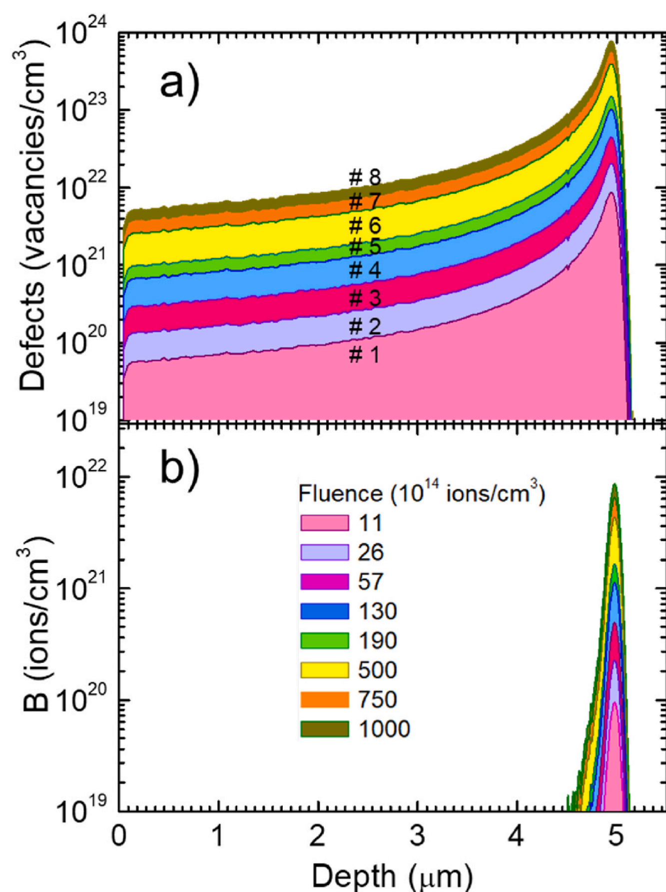

Fig. 2. Results of the SRIM simulations for 9 MeV boron ions implanted on a diamond sample at the indicated values of fluence. (a) Density of vacancies versus depth where the numbers correspond to the stripe in Table 1. (b) Concentration of implanted boron ions versus depth. The fluence for each curve is given in units of 10^{14} ions/cm^2. (A colour version of this figure can be viewed online.)

μm and a length of 500 μm. Possible contribution of a serial contact resistance was neglected.

2.6. Structural characterization (ion channeling and X-ray diffraction)

Ion channeling is a well-established technique to measure implantation damage in combination with Rutherford backscattering spectrometry (RBS/C) or other ion beam methods. Thus, we performed RBS/C experiments using a 1048 keV H^+ beam (1 mm^2 spot) to determine the damage recovery of the sample. Backscattered ions were detected with two silicon barrier detectors placed at 170° and 155° in IBM geometry. A 3-axes goniometer was employed to control the crystal orientation with respect to the probing beam with an accuracy of 0.01°. Angular scans across <100> axis were recorded in steps of 0.05°. Random spectra with a charge of 5 μC were acquired by off-axis rotation of the sample during the measurement. In these experiments, defocused B ions of 8 MeV were previously irradiated, with a fluence of 5.3 × 10^{16} cm^{-2} producing a peak vacancy density of 3.74 × 10^{23} cm^{-3}, that roughly corresponds to the stripe #6.

Complementary information about the crystal quality was obtained by X-ray diffraction (XRD) using a D8 diffractometer (Bruker AXS) with Cu K_α radiation, an asymmetric 4-bounce Ge(220) monochromator, a 0.5 mm collimator and a position sensitive Si strip detector. 2θ/ω scans of the 004 reflection were recorded with steps of 0.005° in order to check the presence of strain along the implantation axis.

3. Results and discussion

3.1. 2D micro-Raman spectroscopy

Micro-Raman mapping experiments were performed to obtain the distribution and evolution of the diamond Raman peak located at 1332 cm^{-1} and of defect peaks that arise due to sample irradiation and to subsequent temperature treatments, as for instance graphite Raman peaks or photoluminescence bands related to created defects. From the collected hyperspectral data, 2D Raman images are then obtained for the intensity and position of the different features for all the regions. These Raman images allow to observe the extension and distribution of the induced defects, as well as the degree of recovery with the annealing treatments. From the whole set of applied fluences, two representative fluences (see Table 1) have been selected in most cases to illustrate the irradiation damage, one with low fluence, around the most conservatively estimated [25–27] threshold of vacancies for graphitization (stripe #2, <2 × 10^{22} cm^{-3}) and one with higher fluence, above the highest reported thresholds [29] up to date (stripe #6: >3 × 10^{23} cm^{-3}). Raman spectra and 2D maps for all the stripes are shown in the Supplementary Data.

3.1.1. Damage in as-irradiated regions

The defects induced by the implantation of different types of ions in a wide range of fluences have been extensively studied using optical spectroscopies [42–44] and other techniques. However, the exact nature of the generated defects is still not fully clear in several cases. The type of implanted particle and the fluence are both relevant parameters for the type and degree of damage in the diamond lattice, as well as in its healing by annealing treatments. The main defects detected in implanted CVD high quality diamond are vacancies, interstitials, amorphization and, after high temperature treatments, graphitization. Here we focus on the distribution of the damage inside and around the boron irradiated region and the recovery depending on the fluence and temperature.

The most evident result of ion implantation is the weakening in intensity and/or loss of the diamond Raman peak, which indicates the amorphization suffered in the implanted areas. Besides, a relevant feature is the appearance of a peak at about 650 cm^{-1} which is a PL band with a wavelength of 503.9 nm related to defects generated in the diamond lattice (Fig. 3 collects several characteristic and representative spectra). This PL band is usually related to the 3H defects reported in irradiated diamond. This defect shows an absorption line at about 503.6 nm (2.462 eV) and an associated PL band at 503.8 nm and is thought to be originated by self-interstitial carbon that is produced by natural or artificial irradiation [45–47]. However, the exact nature (single or bi-interstitial), configuration and charge of this defect are still not clear [48].

In order to visualize the distribution of the irradiation damage, intensity maps of the 1332 cm^{-1} diamond Raman peak and of the 503.9 nm PL band are presented in Fig. 4 for the stripes #2 and #6 (see section 2.4. for the details of the measurements and maps). Since the background in some damaged areas becomes very important (in Fig. 3c the background intensity is similar or even higher than the diamond peak intensity of the pristine sample in Fig. 3a), it has been subtracted for a clear evaluation of the diamond peak intensity.

At low fluences (stripe #2) the diamond peak is still observable within the irradiated region, together with an intense band at 650 cm^{-1} (PL at 503.9 nm). The damaged region looks like an ellipsoidal-shaped capsule well inside the diamond sample centred at about 5 μm inside the sample from the edge where boron ions are implanted (Fig. 4, stripe #2). This encapsulation begins to fail at higher fluences (stripe #3 and above). High fluences (stripe #5 and above) result in higher damage in the diamond sample and the damaged regions clearly exceed the expected area centred about 5 μm deep from the sample edge. The damaged/amorphous region begins at the edge of the sample and loses

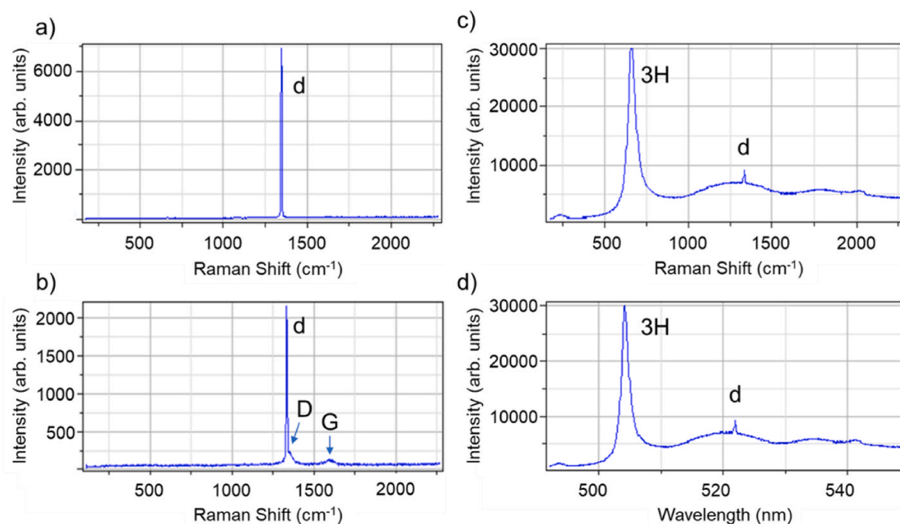

Fig. 3. Representative spectra: a) pristine diamond (d = diamond peak), b) irradiated region after 1200 °C annealing showing small graphite peaks (D and G); c) and d) spectra close to an as-irradiated region showing the 3H PL band (c) in Raman shift and (d) in nm. (A colour version of this figure can be viewed online.)

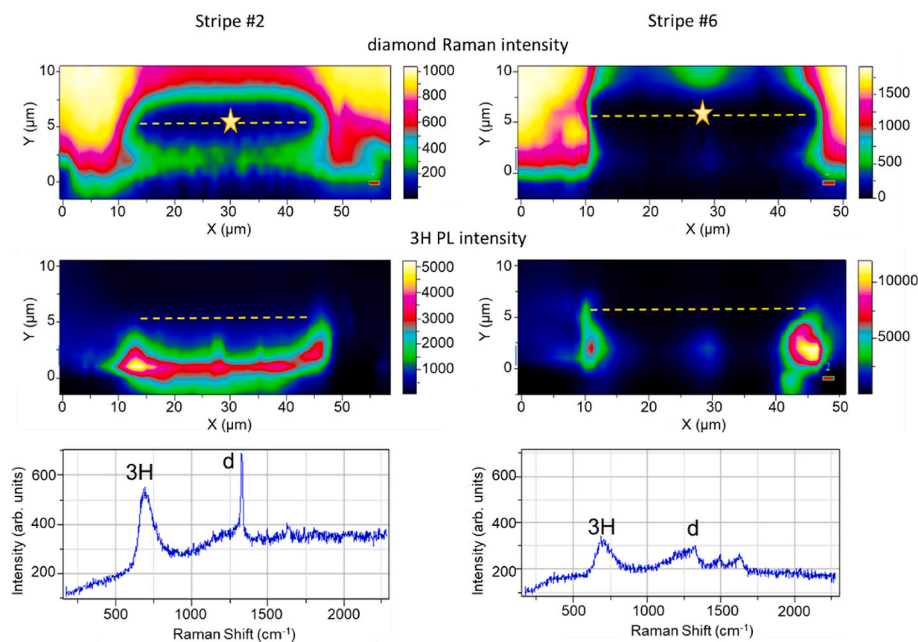

Fig. 4. Comparison of the images of the diamond peak intensity (higher panels) and 3H PL intensity (lower panels) for stripe #2 (left) and #6 (right). The horizontal dashed lines indicate the location of the implanted boron according to SRIM simulations. The spectra correspond to boron implanted position indicated with yellow stars for stripes #2 and #6. (A colour version of this figure can be viewed online.)

its "capsule" shape as it is shown by monitoring the intensity of the diamond peak (Fig. 4, stripe #6). The amorphous region extends deeper in the diamond lattice by several microns while the 3H defects are detected laterally also few microns outwards. The location of 3H defects at the edges of the implantation region have also been reported for other ions [49]. Both are indications of the migration of the radiation-induced defects. Since the intensity of the diamond peak is proportional to the volume of regular diamond in the laser spot, the intensity reduction can be used as an estimation of the degree of amorphization. In stripe #2, the green colour in Fig. 4 corresponds to regions where approximately 50% of the diamond has been amorphized and, in the implantation region with the highest damage, the fraction of remaining diamond is reduced to around 2%. As the fluence increases, the amorphous region increases along the implantation direction reaching the edge of the sample while it is limited in depth to around 2−3 μm deeper than the B location. At this stage no graphite peaks are detected, as expected.

On the other hand, the PL band related to 3H defects is high within the volume irradiated with boron for the lower fluence stripes, while for higher fluences they are located on the outer edges of the irradiated volume (Fig. 4). Very faint traces of the 3H band can be found inside the irradiated region. In parallel to the well-defined 3H PL band, the background increases substantially (Fig. 3 c and d, see scales) with a behaviour totally parallel to that of the 503.9 nm band (see Fig. S1). Thus, the origin of the electronic transitions originating this photoluminescence background is related to the 3H defects. The spatial localization of the 3H PL band and its dependence on the fluence are indicating that the lower damage induced by boron irradiation is the displacement of carbon atoms from their regular position in the diamond lattice to interstitial sites. Heavier fluences finally lead to the amorphization of the diamond, so that the 3H band is never seen when the

diamond peak is strongly depleted. In a previous work, where P was implanted in diamond, regions with nanometric amorphous C (a-C) dots embedded in the diamond lattice have been detected at the surface and beyond the implantation depth of P using High-resolution transmission electron microscopy (HRTEM) [50], while fully amorphous carbon is observed in between. This indicates that, after the formation of vacancies and interstitials, the damage begins to nucleate forming a-C nanodots that probably grow in size as the ion implantation proceeds, leaving pristine diamond regions. For the highest fluences (stripes #6−#8) diamond is totally transformed into amorphous C in extended areas.

3.1.2. Annealing recovery

In order to recover the integrity of the sample in the irradiated regions, two successive annealing treatments were applied, as described in section 2.3., the first one at 1000 °C. After annealing, micro-Raman experiments on the same regions and conditions were performed. Fig. 5 presents again the intensity maps for the diamond Raman peak (1332 cm^{-1}) and for the 3H PL band (503.9 nm) corresponding to same stripes #2 and #6, as in Fig. 4, after the annealing in vacuum at 1000 °C.

Regions irradiated with low fluences experience a clear improvement of the diamond peak intensity in the damaged region (as for instance in case of stripe #2 in Fig. 5). Where there was a very faint diamond peak (2%), now the diamond fraction reaches around 60% (see spectra in the lower part of the figures). The 3H PL band also disappears in the irradiated region and only some remnants near the lateral edges can be witnessed. In the case of high fluences (for instance stripe #6 in Fig. 5) the damaged region shrinks, recovering the diamond peak but yet with lesser intensity (from no diamond peak to around 20% in the implantation region). The 3H PL band is only seen in the lateral edges of the damaged area and its intensity is drastically reduced (see the scales). The 1000 °C annealing procedure results in an improvement of the damaged region (recuperation of the diamond peak and reduction of the 3H defects) whose degree strongly depends on the fluence. It is to note that no graphite peaks can be observed after this annealing even for the highest fluence. However, since the sample does not return to the initial situation before irradiation, a second annealing procedure at 1200 °C was undertaken.

In the case of low fluences, this new annealing at 1200 °C results in a slight reduction of the damaged region, but without really improving the intensity of the diamond Raman peak (see Figs. S2 and S3 for more information). In the case of high fluences, the diamond peak is not further recovered, indeed, it is even depleted below the B implantation depth ($y < 5$ µm, Fig. S3). On the contrary, the 3H PL band is drastically reduced so the edge zones are almost totally recovered (see the scales of 3H band intensity images for stripe #6 in Fig. S2). Extremely low densities of C interstitials are detected in lateral positions far from the irradiated regions, indicating that the 1200 °C annealing induces the diffusion of the remaining 3H defects outwards of the implanted area (in Fig. S2, see image for 3H defects after 1200 °C annealing). Moreover, even after the 1200 °C annealing it is still possible to detect a PL band at 740 nm that may have the same origin as the PL band reported at 741 nm measured at 7K and assigned to the luminescence of isolated neutral vacancies (GR1) [51]. Fig. 6 shows that the vacancies (740 nm band) remain in the trajectory of the boron ions while the interstitials are located at both sides of this region demonstrating the migration of C outside the irradiated regions.

After the 1200 °C annealing treatments, very weak graphite peaks [52] at around 1350 and 1600 cm^{-1} (D and G Raman peaks of graphite) are detected for the stripes #3, #5, #6 and #8, but not for #1, #2, #4 and #7 (Fig. 7 and Fig. S5). The graphite distribution is inhomogeneous in any case. Surprisingly, the appearance of graphitization features does not clearly correlate with the fluence within the studied range. In brief, we can state that graphitization of the amorphized regions of diamond after high boron-ion fluences has been totally avoided for 1000 °C annealing and occasional zones with very weak graphite Raman signal are detected for 1200 °C. Interestingly, after annealing at 1350 °C Aprà et al. [53] observed an area partially graphitized in B-implanted diamond at 8 MeV with an ion-induced damage at the peak from about 4.4 $\times 10^{22}$ vacancies cm^{-3}, which roughly coincides with our stripe #3 (4.37 $\times 10^{22}$ vacancies cm^{-3}), the stripe of lower damage where the Raman graphite peaks have been detected in this study.

The position and width of the diamond peak can be modified when the diamond lattice is distorted/strained or diamond nanodots are formed. Also, the presence of defects can enhance anharmonic relaxation producing frequency softening and peak widening that can be used

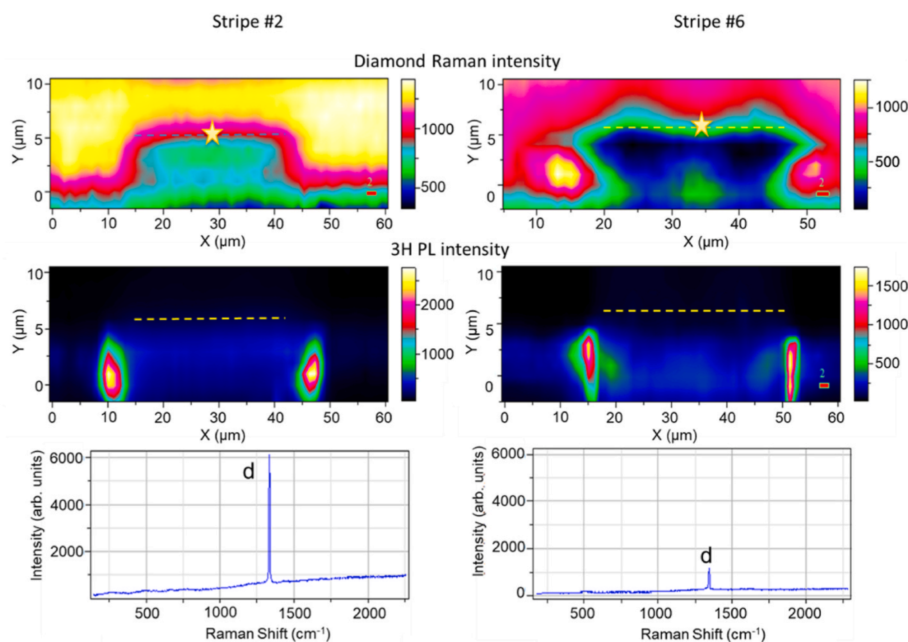

Fig. 5. Comparison of the images of the diamond peak intensity (higher panels) and 3H PL intensity (lower panels) for stripe #2 (left) and #6 (right) after the annealing at 1000 °C. The horizontal dashed lines indicate the location of the implanted boron according the SRIM simulations. The spectra correspond to boron implanted position indicated with yellow stars for stripes #2 and #6. (A colour version of this figure can be viewed online.)

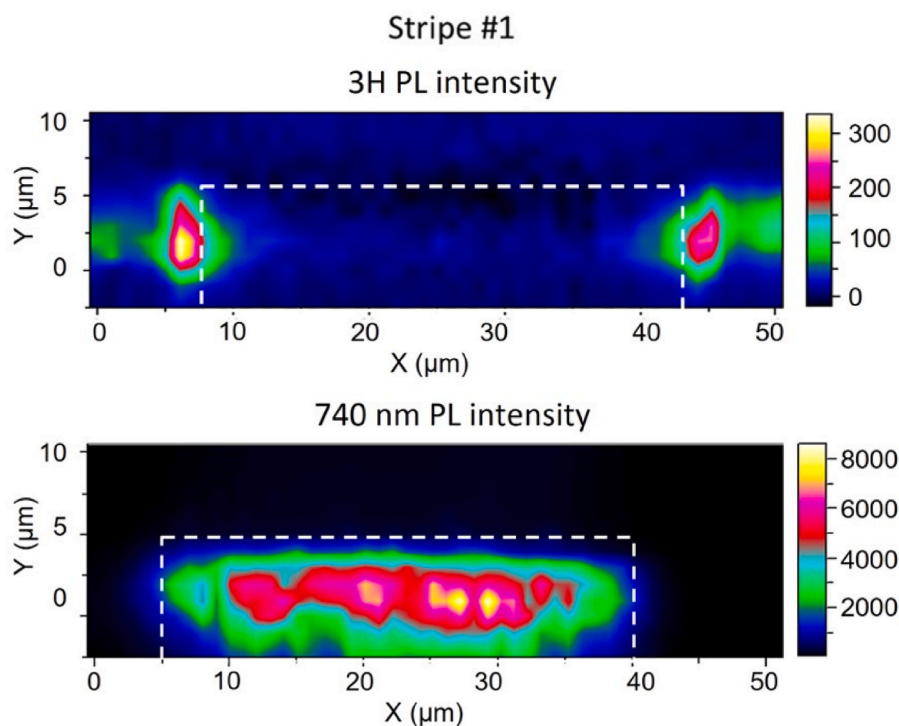

Fig. 6. Intensity maps of the PL bands related to: a) the 3H defects, at 503.9 nm, and b) the vacancies, at 740 nm, after the 1200 °C annealing of stripe #1. (A colour version of this figure can be viewed online.)

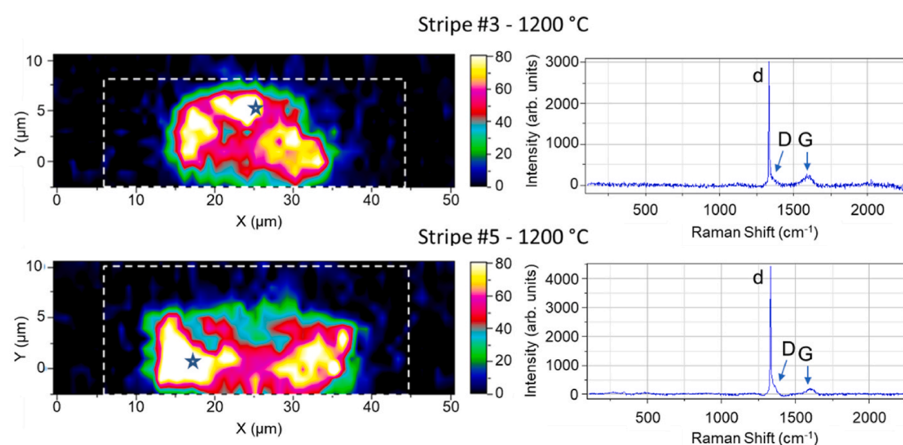

Fig. 7. Left: Images of the graphite 1600 cm^{-1} G-peak intensity after 1200 °C annealing, in stripes #3 and #5. The dashed line rectangles indicate the areas of large diamond intensity reduction in the same stripes of the as-implanted sample. Right: Spectra corresponding to the position indicated with a star for each stripe. (A colour version of this figure can be viewed online.)

to estimate the defect concentration [29]. As previously reported, the position of the diamond peak downshifts and broadens to some extent with the damage produced by boron and carbon implantation [34,35]. Here we analyze the distribution of the damage using 2D images of the positions of the diamond peak (Fig. 8). For stripe #2 the diamond peak is slightly down-shifted (2 cm^{-1}) in a region that begins at the edge of the sample and reaches the boron implantation depth, but, for higher fluences, the modifications are larger (up to 12 cm^{-1}) and extend beyond the irradiated area as side lobes (rightside column in Fig. 8). Similar lobes are also seen as bright regions in crossed polarized images which can be interpreted as being originated by the induced strain upon implantation. Moreover, no clear widening of the Raman peak can be appreciated except for the extremely amorphized regions where the diamond peak blends into the background. These observations are indications that the swelling of the lattice induced by the ion implantation process is an important factor for the observed frequency decrease. Interestingly, within the regions where the 3H defect appears (Fig. 4) the diamond peak is unmodified suggesting that the formation of 3H defects does not significantly modify the C–C bonds in the diamond lattice. For stripe #2 the regular position of the diamond peak is totally recovered after 1000 °C annealing, while this is not the case for high fluences (stripe #6), where a significant but partial recovery is observed.

Regarding the Raman diamond peak, an improvement in quality is clearly achieved after the first annealing (1000 °C), but the second annealing is detrimental for high fluences. For some fluences, the second annealing procedure even reduces slightly the intensity of the diamond Raman peak. In fact, after this annealing procedure, some material of the surface of the irradiated region has been lost, more evidently in the high

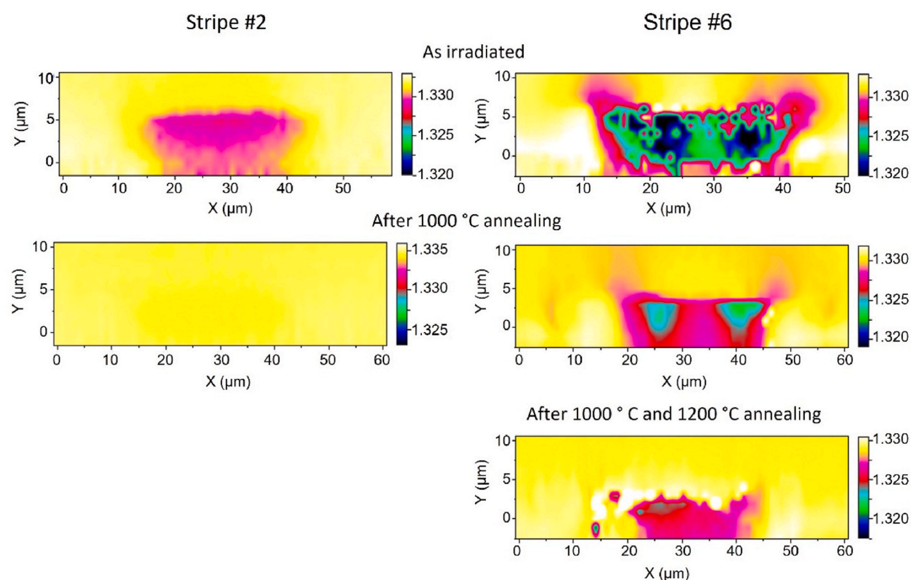

Fig. 8. Raman images of the position of the diamond Raman peak for stripes #2 and #6 in the as-irradiated sample, after annealing at 1000 °C and after the second annealing at 1200 °C (for stripe #6). The yellow color corresponds to the regular position of diamond. The frequency intervals (right scales of the images) are in all cases 13 cm^{-1}. (A colour version of this figure can be viewed online.)

fluence stripes (#7 and #8). Finally, small traces of graphite phase were occasionally found to coexist with crystalline and disordered diamond phases, though uncorrelated with the used fluence and only after annealing at 1200 °C.

In summary, the graphitization, which is induced by high-temperature annealing of the previously amorphized regions, depends in an intricate and yet not well-known manner, on the implanted ion, the fluence, the purity and quality of the diamond and, especially, on the annealing temperature. Finally, the possibility of performing combined high-pressure and high-temperature (HPHT) annealing can also be considered as an activation method for ion-implanted dopants in diamond [54].

3.2. Electrical resistivity at low temperatures

The electrical resistivity ρ of different stripes in several samples was measured at low temperatures. In all cases, ρ increased with decreasing temperature, and in none of them any hint of a superconducting transition was observed even below liquid helium temperatures. In Fig. 9, a selection of representative measurements is presented. Specifically, data for the highly-doped stripes #6 and #8, both after 1000 °C and after 1200 °C annealing, are shown. The irradiated samples annealed at 1000 °C exhibit a semimetallic behaviour akin to that observed in HPHT and CVD grown crystals of boron-doped diamond [10–13], with the exception of the superconducting transition. However, after annealing at 1200 °C the irradiated stripes exhibit a semiconducting-like behaviour, though with a saturation of the resistivity at lower temperatures, which may be related to carriers from ionized impurity levels as found in other materials [55,56].

Therefore, although ion-beam implanted BDD presents after annealing at 1000 °C electrical resistivity curves similar to those found in samples grown by other methods, it seems unable to produce superconductivity. Further annealing at 1200 °C appears to be detrimental to the electrical conductivity, which decreases orders of magnitude. This is consistent with the observation by Raman spectroscopy of the important diamond lattice healing after the 1000 °C annealing and its deterioration after the 1200 °C one for the high irradiation fluence of stripe #6.

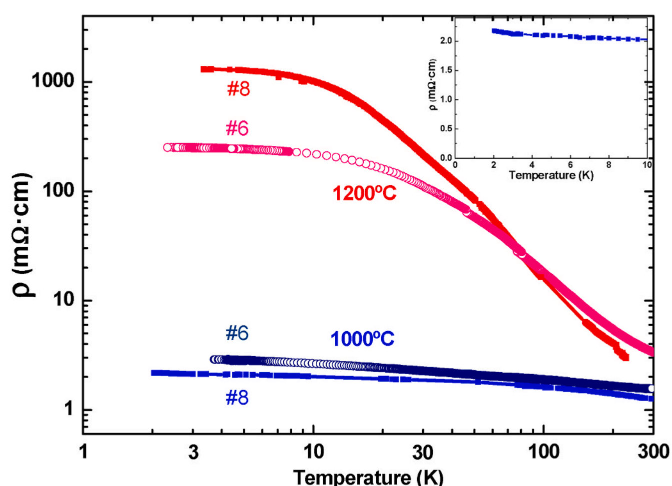

Fig. 9. Electrical resistivity curves as a function of temperature for irradiated stripes #6 and #8 (see Table 1), after annealing at 1000 °C (blue symbols) and after annealing at 1200 °C (red symbols). Inset: amplification in a linear scale of the ρ(*T*) curve at the lowest temperatures for the best conducting sample, namely stripe #8 annealed at 1000 °C. No superconductivity hint is observed down to 2 K. (A colour version of this figure can be viewed online.)

3.3. Structural characterization (ion channeling and X-ray diffraction)

Fig. 10a shows the RBS/C angular scans along the <100> axis for a sample in both virgin and implanted (and further annealed at 1200 °C) states. As specified in section 2.6., B ions at 8 MeV were irradiated, with a fluence to produce the same damage as in stripe #6. In the angular scans the statistics for the B signal was below the level of detection and, thus, the lattice-site location of this element was not feasible.

The minimum yield (χ_{min}), defined as the ratio between the random and the aligned yield, is the main parameter revealing the crystal quality. In this regard, it is worth noticing that the χ_{min} = 25% of the virgin sample is considerably higher than that expected for bulk crystals (typically below 10% [57]). This might indicate a relatively high amount of native defects. In order to check this fact, XRD experiments were also conducted. Specifically, we performed ω rocking curves in the

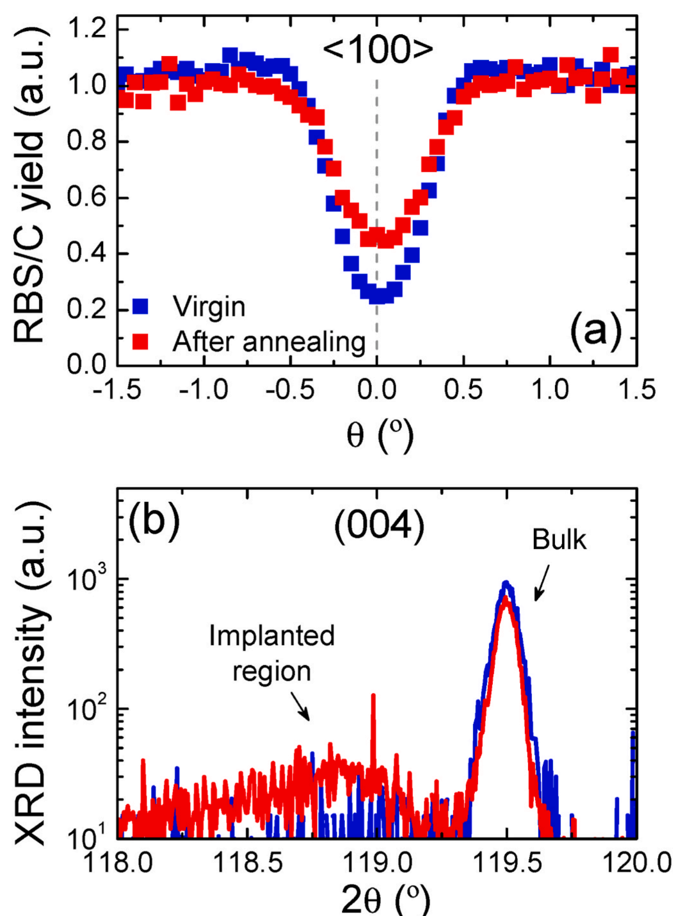

Fig. 10. (a) RBS/C angular scan along the <100> axis for a sample both in virgin and implanted + annealed states. The minimum yield of the dips shows a partial but incomplete recovery of the implantation damage. (b) XRD 2θ/ω scan in the (004) reflection for the same sample: virgin (blue line); implanted and annealed at 1200 °C (red line). The peak at 119.5° indicates the native lattice parameter of the material, while the broad band at 118.8° reflects the remaining presence of strain in the implanted region. (A colour version of this figure can be viewed online.)

(220) and (004) planes, obtaining a FWHM of 48.6 and 51.7 arcsec, respectively. These values are comparable to those of the literature [58]. However, since both XRD and RBS/C have different sensitivities to defects (e.g., domains or interstitials), further research is needed to clarify the origin of this χ_{min} value.

Regarding the implanted and annealed sample, we found χ_{min} = 44%, demonstrating that annealing at 1200 °C is not adequate to fully recover the implantation damage for high fluences, as also observed by Raman spectroscopy. This effect is also contrasted with 2θ/ω scans in the (004) plane of the crystals (Fig. 10b). Both a decrease in the main peak (at 2θ = 119.5°) and an increase of the intensity in the lower band at 118.8° peak are clearly visible. These features indicate a reduction of the crystal quality and the presence of strain induced by the implantation. Specifically, the lattice parameter is estimated to change from 0.3567 nm (virgin) to 0.3580 nm (after irradiation and annealing at 1200 °C), i.e., the produced strain is 0.364%. Therefore, this strain, which is a common feature of ion implantations even at relatively low fluences [59], has been removed only partially in our samples. This fact agrees well with the high χ_{min} detected and the incomplete recovery after the annealing. Furthermore, the observed expansion of the lattice parameter correlates well with the decrease of the Raman peak frequency of diamond, since the detected 0.364% variation of the lattice parameter produces a proportional reduction (this rude approximation justified by the very small strain) of ~5 cm^{-1} in the Raman peak, in good agreement with the observed behaviour for stripe #6 after annealing in Fig. 8, and in general for the implantations with the highest fluences.

4. Conclusions

We have performed an exhaustive set of micrometric irradiations on single crystals of ultrapure diamond with boron ions of 9 MeV, using ion fluences in a wide range, to study the damage and eventual recovery after annealing in the differently implanted regions by means of complementary characterization techniques.

It was found that, although amorphization of the diamond crystal was apparent in many of the stripes, a significant recovery into the diamond crystalline lattice was observed instead of graphitization for nominal vacancy densities about ~7 × 10^{23} vacancies/cm^3 in almost the entire irradiated volume. This is in clear contrast to earlier reports, but it agrees and builds on other works using MeV He^+ ions, which observed an increase in the graphitization threshold for diamond, attributed to the effect of the "internal pressure" that avoids an expansion to the graphite structure in deeply buried amorphized regions. In short, the graphitization of damaged diamond after annealing depends on many factors (irradiated ion, implantation depth, annealing temperature, etc.), what explains the very different graphitization thresholds found in the literature.

Interestingly, the damage induced by B implantation is found to extend well beyond the region of vacancy formation calculated by SRIM. B implantation induces the formation of C vacancies and C interstitials that result in a varying amorphization degree and extension depending on the fluence. At not too high fluences (≤5 × 10^{16} cm^{-2}) or vacancy densities (roughly for <5 × 10^{23} cm^{-3}), C atoms are displaced from the path and position where B is implanted (5 μm deep), eventually producing a hybrid amorphous/crystalline region, while C interstitials are found along the B path and at the edges. Annealing allows for an almost complete recovery of the diamond lattice while maintaining some vacancy concentration along the B path and interstitials at the edges. High fluences increase the amorphous fraction and area, whereas interstitials are relegated to contiguous regions (edges), evidencing the C migration from the B path, where the strain of the diamond lattice is maximized. Partial diamond-lattice recovery is obtained by annealing at 1000 °C with no graphitization. Only a second treatment at 1200 °C does produce a small graphite fraction with no clear correlation with the B fluence. The recovery of the diamond lattice is accomplished by the thermally activated diffusion of the C interstitials from the adjacent regions towards the B implantation path and B location. Strain is consequently drastically reduced. Annealing at 1200 °C for high fluences is detrimental for the diamond lattice compared to that at 1000 °C and produces a small density of graphite nanodots. The increased quality of the diamond lattice at 1000 °C that worsens afterwards at 1200 °C correlate with the observed electric conductivity behaviour. In brief, the 1000 °C annealing produces an optimal recovery of the diamond in the highly irradiated regions and a total recovery in the lightly damaged regions, while 1200 °C is detrimental in terms of diamond healing within the boron trajectory region and with the formation of small fractions of graphite. Thus, 1000 °C is the adequate annealing temperature for diamond recovery in this case. Using a different strategy, Creedon et al. [60] were able to suppress superconductivity in CVD-grown BDD crystals with T_c = 8 K by introducing compensating defects via 1-MeV He ions. Interestingly, superconductivity was partially recovered (T_c = 4 K) after annealing at 1150° and worsened (T_c = 2.2 K) after further annealing at 1250°.

Despite the serious problem of graphitization has been overcome below the minimum detectable limit for the 1000 °C annealing and to a great extent for 1200 °C in our work, the produced boron-doped diamond does not exhibit superconductivity, at least above 2 K. Firstly, this could be associated with the ion-beam implanted boron occupying the diamond lattice as an interstitial and not substitutionally replacing one C

position in the diamond lattice, thereby modifying the expected conditions for superconductivity in BDD. Nonetheless, as discussed in the introduction, other recent works have postulated that superconductivity in BDD is of a granular character and uncorrelated with boron concentration [15,16]. Also, the observation of superconductivity in some types of amorphous carbon with much higher critical temperatures [18,19] casts doubt about the more traditional BCS-like explanation of superconductivity in BDD. As a matter of fact, the role played by the wide range of defects present in crystalline carbon, as well as the induced disorder, is probably very relevant, although it is not yet well understood.

Therefore, possible research lines for the future range from envisaging different irradiation protocols and strategies to get the boron substitutional in the diamond lattice to irradiate different types of diamond, including polycrystalline samples or heavily damaged or amorphized diamond.

CRediT authorship contribution statement

R.J. Jiménez-Riobóo: Investigation, Formal analysis, Visualization, Writing – review & editing. **N. Gordillo:** Investigation, Formal analysis, Visualization, Writing – review & editing, Funding acquisition. **A. de Andrés:** Conceptualization, Visualization, Writing – original draft, Funding acquisition. **A. Redondo-Cubero:** Investigation, Formal analysis, Writing – review & editing. **M. Moratalla:** Investigation, Formal analysis. **M.A. Ramos:** Conceptualization, Investigation, Writing – original draft, Funding acquisition. **M.D. Ynsa:** Conceptualization, Investigation, Writing – review & editing, Funding acquisition.

Declaration of competing interest

The authors declare that they have no known competing financial interests or personal relationships that could have appeared to influence the work reported in this paper.

Acknowledgements

This work has been partially supported by the Ministerio de Ciencia e Innovación of Spain (Project grants PID2020-112770RB-C22/MCIN/AEI/10.13039/501100011033, PID2021-127033OB-C21/MCIN/AEI/10.13039/501100011033, and PID2021-127498NB-I00/AEI/FEDER/10.13039/501100011033). We also acknowledge financial support from MCIN/AEI/10.13039/501100011033, through the "María de Maeztu" Programme for Units of Excellence in R&D (CEX2018-000805-M), as well as from the Autonomous Community of Madrid through program S2018/NMT-4321 (NANOMAGCOST-CM).

We thank the technical staff of CMAM for operating the ion-beam accelerator, Gastón García for a critical reading of the manuscript, and Jose María Castilla for his support in low-temperature measurements. M.A.R. gratefully acknowledges interesting discussions with Pablo Esquinazi.

Appendix A. Supplementary data

Supplementary data to this article can be found online at https://doi.org/10.1016/j.carbon.2023.04.004.

References

[1] M.A. Prelas, G. Popovici, L.K. Bigelow, Handbook of Industrial Diamonds and Diamond Films, Marcel Dekker Inc., New York, 1998.
[2] A.M. Zaitsev, Optical Properties of Diamond, Springer-Verlag, Berlin, 2001, https://doi.org/10.1007/978-3-662-04548-0.
[3] F. Fontaine, E. Gheeraert, A. Deneuville, Conduction mechanisms in boron implanted diamond films, Diam. Relat. Mater. 5 (1996) 752–756, https://doi.org/10.1016/0925-9635(95)00383-5.
[4] J.F. Prins, Using ion implantation to dope diamond – an update on selected issues, Diam. Relat. Mater. 10 (2001) 1756–1764, https://doi.org/10.1016/S0925-9635(01)00427-7.
[5] T. Vogel, J. Meijer, A. Zaitsev, Highly effective p-type doping of diamond by MeV-ion implantation of boron, Diam. Relat. Mater. 13 (2004) 1822–1825, https://doi.org/10.1016/j.diamond.2004.04.005.
[6] D. Sang, H. Li, S. Cheng, Q. Wang, J. Liu, Q. Wang, S. Wang, C. Han, K. Chen, Y. Pan, Ultraviolet photoelectrical properties of a n-ZnO nanorods/p-diamond heterojunction, RSC Adv. 5 (2015) 49211–49215, https://doi.org/10.1039/C5RA06054K.
[7] H. Li, S. Cheng, J. Li, J.A. Song, A review on the low-dimensional and hybridized nanostructured diamond films, J. Nanomater. 2015 (2015), 692562, https://doi.org/10.1155/2015/692562.
[8] T. Tshepe, C. Kasl, J.F. Prins, M.J.R. Hoch, Metal-insulator transition in boron-ion-implanted diamond, Phys. Rev. B 70 (2004), 245107, https://doi.org/10.1103/PhysRevB.70.245107.
[9] T. Klein, P. Achatz, J. Kacmarzik, C. Marcenat, F. Gustafsson, J. Marcus, E. Bustarret, J. Pernot, F. Omnes, Bo E. Sernelius, C. Persson, A. Ferreira da Silva, C. Cytermann, Metal-insulator transition and superconductivity in boron-doped diamond, Phys. Rev. B 75 (2007), 165313, https://doi.org/10.1103/PhysRevB.75.165313.
[10] E.A. Ekimov, V.A. Sidorov, E.D. Bauer, N.N. Melnik, N.J. Curro, J.D. Thompson, S. M. Stishov, Superconductivity in diamond, Nature 428 (6982) (2004) 542–545, https://doi.org/10.1038/nature02449.
[11] Y. Takano, M. Nagao, I. Sakaguchi, M. Tachiki, T. Hatano, K. Kobayashi, H. Umezawa, H. Kawarada, Superconductivity in diamond thin films well above liquid helium temperature, Appl. Phys. Lett. 85 (14) (2004) 2851–2853, https://doi.org/10.1063/1.1802389.
[12] E. Bustarret, J. Kačmarčik, C. Marcenat, E. Gheeraert, C. Cytermann, J. Marcus, T. Klein, Dependence of the superconducting transition temperature on the doping level in single-crystalline diamond films, Phys. Rev. Lett. 93 (2004), 237005, https://doi.org/10.1103/PhysRevLett.93.237005.
[13] Y. Takano, M. Nagao, T. Takenouchi, H. Umezawa, I. Sakaguchi, M. Tachiki, H. Kawarada, Superconductivity in polycrystalline diamond thin films, Diam. Relat. Mater. 14 (2005) 1936–1938, https://doi.org/10.1016/j.diamond.2005.08.014.
[14] H. Okazaki, T. Wakita, T. Muro, T. Nakamura, Y. Muraoka, T. Yokoya, S. Kurihara, H. Kawarada, T. Oguchi, Y. Takano, Signature of high T_c above 25 K in high quality superconducting diamond, Appl. Phys. Lett. 106 (2015), 052601, https://doi.org/10.1063/1.4907411.
[15] G. Zhang, et al., Global and local superconductivity in boron-doped granular diamond, Adv. Mater. 26 (2014) 2034–2040, https://doi.org/10.1002/adma.201304667.
[16] G. Zhang, et al., Bosonic anomalies in boron-doped polycrystalline diamond, Phys. Rev. Appl. 6 (2016), 064011, https://doi.org/10.1103/PhysRevApplied.6.064011.
[17] N. Murata, J. Haruyama, J. Reppert, A.M. Rao, T. Koretsune, S. Saito, M. Matsudaira, Y. Yagi, Superconductivity in thin films of boron-doped carbon nanotubes, Phys. Rev. Lett. 101 (2008), 027002, https://doi.org/10.1103/PhysRevLett.101.027002.
[18] A. Bhaumik, R. Sachan, J. Narayan, High-temperature superconductivity in boron-doped Q-carbon, ACS Nano 11 (2017) 5351–5357, https://doi.org/10.1021/acsnano.7b01294.
[19] J. Narayan, A. Bhaumik, R. Sachan, High-Temperature superconductivity in distinct phases of amorphous B-Doped Q-Carbon, J. Appl. Phys. 123 (2018), 135304, https://doi.org/10.1063/1.5016397.
[20] V. Heera, R. Höhne, O. Ignatchik, H. Reuther, P. Esquinazi, Absence of superconductivity in boron-implanted diamond, Diam. Relat. Mater. 17 (2008) 383, https://doi.org/10.1016/j.diamond.2008.01.057.
[21] L.H. Willems van Beveren, R. Liu, H. Bowers, K. Ganesan, B.C. Johnson, J. C. McCallum, S. Prawer, Optical and electronic properties of sub-surface conducting layers in diamond created by MeV B-implantation at elevated temperatures, J. Appl. Phys. 119 (22) (2016), 223902, https://doi.org/10.1063/1.4953583.
[22] S. Prawer, K. Nugent, D. Jamieson, The Raman spectrum of amorphous diamond, Diam. Relat. Mater. 7 (1998) 106–110, https://doi.org/10.1016/S0925-9635(97)00194-5.
[23] G. García, M. Díaz-Hijar, V. Tormo-Márquez, I. Preda, O. Peña-Rodríguez, J. Olivares, Structural damage on single-crystal diamond by swift heavy ion irradiation, Diam. Relat. Mater. 58 (2015) 226–229, https://doi.org/10.1016/j.diamond.2015.08.014.
[24] G. García, M. Martin, M.D. Ynsa, V. Torres-Costa, M.L. Crespillo, M. Tardío, J. Olivares, F. Bosia, O. Peña-Rodríguez, J. Nicolas, M. Tallarida, Process design for the manufacturing of soft X-ray gratings in single-crystal diamond by high-energy heavy-ion irradiation, Eur. Phys. J. Plus 137 (2022) 1157, https://doi.org/10.1140/epjp/s13360-022-03358-3.
[25] C. Uzan-Saguy, C. Cytermann, R. Brener, V. Richter, M. Shaanan, R. Kalish, Damage threshold for ion-beam induced graphitization of diamond, Appl. Phys. Lett. 67 (9) (1995) 1194–1196, https://doi.org/10.1063/1.115004.
[26] R. Kalish, A. Reznik, S. Prawer, D. Saada, J. Adler, Ion-implantation-induced defects in diamond and their annealing: experiment and simulation, Phys. Status Solidi A 174 (1) (1999) 83–99, https://doi.org/10.1002/(SICI)1521-396X(199907)174:1<83::AID-PSSA83>3.0.CO;2-3.
[27] R. Kalish, A. Reznik, K.W. Nugent, S. Prawer, The nature of damage in ionimplanted and annealed diamond, Nucl. Instrum. Methods Phys. Res., Sect. B 148 (14) (1999) 626–633, https://doi.org/10.1016/S0168-583X(98)00857-X.

[28] C. Uzan-Saguy, R. Kalish, R. Walker, D.N. Jamieson, S. Prawer, Formation of delta-doped, buried conducting layers in diamond, by high-energy, B-ion implantation, Diam. Relat. Mater. 7 (10) (1998) 1429–1432, https://doi.org/10.1016/S0925-9635(98)00231-3.
[29] J.O. Orwa, K.W. Nugent, D.N. Jamieson, S. Prawer, Raman investigation of damage caused by deep ion implantation in diamond, Phys. Rev. B 62 (9) (2000) 5461–5472, https://doi.org/10.1103/PhysRevB.62.5461.
[30] P. Olivero, S. Rubanov, P. Reichart, B.C. Gibson, S.T. Huntington, J.R. Rabeau, A. D. Greentree, J. Salzman, D. Moore, D.N. Jamieson, S. Prawer, Characterization of three-dimensional microstructures in single-crystal diamond, Diam. Relat. Mater. 15 (10) (2006) 1614–1621, https://doi.org/10.1016/j.diamond.2006.01.018.
[31] B.A. Fairchild, S. Rubanov, D.W.M. Lau, M. Robinson, I. Suarez-Martinez, N. Marks, A.D. Greentree, D. McCulloch, S. Prawer, Mechanism for the amorphisation of diamond, Adv. Mater. 24 (2012) 2024–2029, https://doi.org/10.1002/adma.201104511.
[32] A. Battiato, M. Lorusso, E. Bernardi, F. Picollo, F. Bosia, D. Ugues, A. Zelferino, A. Damin, J. Baima, N.M. Pugno, E.P. Ambrosio, P. Olivero, Softening the ultra-stiff: controlled variation of Young's modulus in single-crystal diamond by ion implantation, Acta Mater. 116 (2016) 95–103, https://doi.org/10.1016/j.actamat.2016.06.019.
[33] M.D. Ynsa, F. Agulló-Rueda, N. Gordillo, A. Maira, D. Moreno-Cerrada, M. A. Ramos, Study of the effects of focused high-energy boron ion implantation in diamond, Nucl. Instrum. Methods B. 404 (2017) 207–210, https://doi.org/10.1016/j.nimb.2017.01.052.
[34] F. Agulló-Rueda, M.D. Ynsa, N. Gordillo, A. Maira, D. Moreno-Cerrada, M. A. Ramos, Micro-Raman spectroscopy of near-surface damage in diamond irradiated with 9-MeV boron ions, Diam. Relat. Mater. 72 (2017) 94–98, https://doi.org/10.1016/j.diamond.2017.01.010.
[35] F. Agulló-Rueda, N. Gordillo, M.D. Ynsa, A. Maira, J. Cañas, M.A. Ramos, Lattice damage in 9-MeV-carbon irradiated diamond and its recovery after annealing, Carbon 123 (2017) 334–343, https://doi.org/10.1016/j.carbon.2017.07.076.
[36] R. Walker, S. Prawer, D.N. Jamieson, K.W. Nugent, Formation of buried p-type conducting layers in diamond, Appl. Phys. Lett. 71 (1997) 1492, https://doi.org/10.1063/1.119946.
[37] S. Prawer, D.N. Jamieson, K.W. Nugent, R. Walker, C. Uzan-Saguy, R. Kalish, MeV ion implantation doping of diamond, MRS Online Proc. Libr. 647 (2000) 43, https://doi.org/10.1557/proc-647-o4.3.
[38] A. Redondo-Cubero, M.J.G. Borge, N. Gordillo, P.C. Gutiérrez, J. Olivares, R. Pérez Casero, M.D. Ynsa, Current status and future developments of the ion beam facility at the centre of micro-analysis of materials in Madrid, Eur. Phys. J. Plus 136 (2021) 175, https://doi.org/10.1140/epjp/s13360-021-01085-9.
[39] M.D. Ynsa, M.A. Ramos, N. Skukan, V. Torres-Costa, M. Jakšić, Highly-focused boron implantation in diamond and imaging using the nuclear reaction ^{11}B(p, α)^{8}Be, Nucl. Instrum. Methods Phys. Res., Sect. B 348 (2015) 174, https://doi.org/10.1016/j.nimb.2014.11.036.
[40] http://www.e6.com/.
[41] J.F. Ziegler, J.P. Biersack, U. Littmark (Eds.), The Stopping and Ranges of Ions in Solids, Pergamon Press, New York, 1985. http://www.srim.org/.
[42] G. Davies, Optical properties of electron-irradiated type ia diamond, Proc. Roy. Soc. Lond. A 336 (1974) 507, https://doi.org/10.1098/rspa.1974.0033.
[43] J. Walker, An optical study of the TR12 and 3H defects in irradiated diamond, J. Phys. C Solid State Phys. 10 (1977) 3031.
[44] S.P. Turaga, et al., Cross-sectional hyperspectral imaging of proton implanted diamond, Appl. Phys. Lett. 115 (2019), 021904, https://doi.org/10.1063/1.5109290.
[45] J. Walker, Optical absorption and luminescence in diamond, Rep. Prog. Phys. 42 (1979) 1605.
[46] J.W. Steeds, T.J. Davis, S.J. Charles, J.M. Hayes, J.E. Butler, 3H luminescence in electron-irradiated diamond samples and its relationship to self-interstitials, Diam. Relat. Mater. 8 (1999) 1847–1852.
[47] J.E. Shigley, C.M. Breeding, Optical defects in diamond: a quick reference chart, Gems Gemol. 49 (2013) 107–111.
[48] I.I. Vlasov, R.A. Khmelnitskii, A.V. Khomich, V.G. Ralchenko, W. Wenseleers, E. Goovaerts, Experimental evidence for charge state of 3H defect in diamond, phys. stat. solidi (a) 199 (2003) 103–107, https://doi.org/10.1002/pssa.200303818.
[49] T. Lühmann, N. Raatz, R. John, M. Lesik, J. Rödiger, M. Portail, D. Wildanger, F. Kleißler, K. Nordlund, A. Zaitsev, J.-F. Roch, A. Tallaire, J. Meijer, S. Pezzagna, Screening and engineering of colour centres in diamond, J. Phys. D Appl. Phys. 51 (2018), 483002, https://doi.org/10.1088/1361-6463/aadfab.
[50] P.-H. Wu, W.-H. Ku, K.-A. Chiu, L. Chang, Radiation damage in (001) diamond induced by phosphorus ion implantation, phys. Stat. solidi (a) 219 (2022), 2100829, https://doi.org/10.1002/pssa.202100829.
[51] K. Wang, J.W. Steeds, Z. Li, H. Wang, Annealing and lateral migration of defects in IIa diamond created by near-threshold electron irradiation, Appl. Phys. Lett. 110 (2017), 152101, https://doi.org/10.1063/1.4980017.
[52] A.C. Ferrari, Raman spectroscopy of graphene and graphite: disorder, electron–phonon coupling, doping and nonadiabatic effects, Solid State Commun. 143 (2007) 47–57, https://doi.org/10.1016/j.ssc.2007.03.052.
[53] P. Aprà, J. Ripoll-Sau, J. Manzano-Santamaría, C. Munuera, J. Forneris, S. Ditalia Tchernij, P. Olivero, F. Picollo, E. Vittone, M.D. Ynsa, Structural characterization of 8 MeV ^{11}B implanted diamond, Diam. Relat. Mater. 104 (2020), 107770, https://doi.org/10.1016/j.diamond.2020.107770.
[54] K. Ueda, M. Kasu, T. Makimoto, High-pressure and high-temperature annealing as an activation method for ion-implanted dopants in diamond, Appl. Phys. Lett. 90 (2007), 122102, https://doi.org/10.1063/1.2715034.
[55] S. Tang, M.S. Dresselhaus, Electronic properties of nano-structured bismuth-antimony materials, J. Mater. Chem. C2 (2014) 4710–4726, https://doi.org/10.1039/C4TC00146J.
[56] Y.-M. Lin, S.B. Cronin, O. Rabin, J.Y. Ying, M.S. Dresselhaus, Transport properties of Bi1−xSbx alloy nanowires synthesized by pressure injection, Appl. Phys. Lett. 79 (2001) 677–679, https://doi.org/10.1063/1.1385800.
[57] T.E. Derry, R.W. Fearick, J.P.F. Sellschop, Ion channeling in natural diamond. Minimum yields, Phys. Rev. B 24 (1981) 3675, https://doi.org/10.1103/PhysRevB.24.3675.
[58] X. Xie, X. Wang, Y. Peng, et al., Synthesis and characterization of high quality {100} diamond single crystal, J. Mater. Sci. Mater. Electron. 28 (2017) 9813–9819, https://doi.org/10.1007/s10854-017-6735-7.
[59] W. Wesch, E. Wendler, Ion Beam Modification of Solids, vol. 61, Springer Series in Surface Sciences, 2016, https://doi.org/10.1007/978-3-319-33561-2.
[60] D.L. Creedon, Y. Jiang, K. Ganesan, A. Stacey, T. Kageura, H. Kawarada, J. C. McCallum, B.C. Johnson, S. Prawer, D.N. Jamieson, Irradiation-induced modification of the superconducting properties of heavily-boron-doped diamond, Phys. Rev. Appl. 10 (2018), 044016, https://doi.org/10.1103/PhysRevApplied.10.044016.